Derived Fields

Eugene Zhang and Vijay Natarajan

Abstract This chapter reviews various methods for multifield visualization that are based on the notion of derived fields. The derived fields are categorized based on properties like the number and type of input fields. Mathematical properties, algorithms, and applications are discussed for each derived field. Correlation and alignment measures are examined for a set of homogeneous fields, including pairwise similarity/dissimilarity measurements. Multifield analysis is also discussed in the context of input fields being the components of the decomposition of another field, possibly of a different type. Finally, research challenges are discussed in the context of the design of multifield analysis and visualization methods based on the concept of derived fields.

1 Introduction

In this chapter we consider the notion of *derived fields* in the context of multifield analysis and visualization. We discuss a categorization based on the number of fields studied, their homogeneity, and the type of relationship between the input fields that is captured by the derived field.

First, given a set of at least two fields of the same type, it is possible to define pairwise similarity and dissimilarity for any two of the fields as well as the global alignment and dependency of the fields considered as a whole. These quantities, namely pairwise similarity/dissimilarity, global alignment, and dependency, are derived quantities that can provide critical information on the input fields. For exam-

Eugene Zhang
School of Electrical Engineering and Computer Science, 2111 Kelley Engineering Center, Oregon State University, Corvallis, OR 97331, USA. e-mail: zhange@eecs.oregonstate.edu

Vijay Natarajan
Department of Computer Science and Automation, Supercomputer Education and Research Center, Indian Institute of Science, Bangalore 560012, India. e-mail: vijayn@csa.iisc.ernet.in

ple, when tracking features in fluid flow datasets, it is often desirable to measure the alignment of a sequence of consecutive time-slices in the data. In Section 2 we will review existing work on pairwise derived fields, *i.e.*, the number of input fields is two. In Section 3 we will consider global alignment and dependency measures for the case when there are more than two input fields.

Another scenario of derived fields in the context of multifield visualization is referred to as decomposition and componentization. In this case, this input may be considered as a single field. However, its key characteristics are revealed by a decomposition into multiple derived fields. The behavior of the input field can be better understood by studying each derived field in the decomposition as well as the interplay among them. An example of this is the well-known *Hodge-Helmholtz decomposition*, where an input vector field is decomposed into the sum of three vector fields: (1) *divergence-free*, (2) *curl-free*, and (3) *harmonic* vector fields. We will review techniques corresponding to this category in Section 4.

2 Pairwise Distances and Correlation Measures

A first step towards capturing the relationships between fields in multifield data is to consider pairwise interactions. In this context we discuss the use of distance measures, similarity measures, and local correlations between two fields.

2.1 Correlation Measures

The correlation coefficient is a standard and popular statistical measure used to determine if two sets of real values are linearly related by comparing their deviations from the respective mean values [4, Chapter 8]. When two scalar functions are sampled at discrete points, the correlation coefficient is computed as

$$\rho = \frac{\sum_{i=1}^{n}(x_i - \bar{x}) \cdot (y_i - \bar{y})}{\sqrt{(\sum_{i=1}^{n}(x_i - \bar{x})^2) \cdot (\sum_{i=1}^{n}(y_i - \bar{y})^2)}}$$

where x_i, y_i are the corresponding values of the two functions and $\bar{x}, \bar{y}$ are the mean values of the two functions. Two scalar functions have a high correlation coefficient if they deviate consistently from their respective mean values *i.e.* if one function takes a value close to its mean then so does the other function at the same point on the domain. Note that the correlation coefficient as defined above is a global measure. However, in the context of two time-varying fields, the correlation coefficient can be computed at each point resulting in a derived field over the domain. This field captures the linear relationship between the two time series data at each point.

Xu et al. [27] track features in a flow dataset by treating the 3D flow field as a stack of 2D vector fields. Given a point in one slice in the stack, points in other slices

can be correlated to this point by treating the 2D vector fields as spin images. This idea is then extended to using the velocity gradient tensor fields of the vector fields, leading to more efficient feature matching.

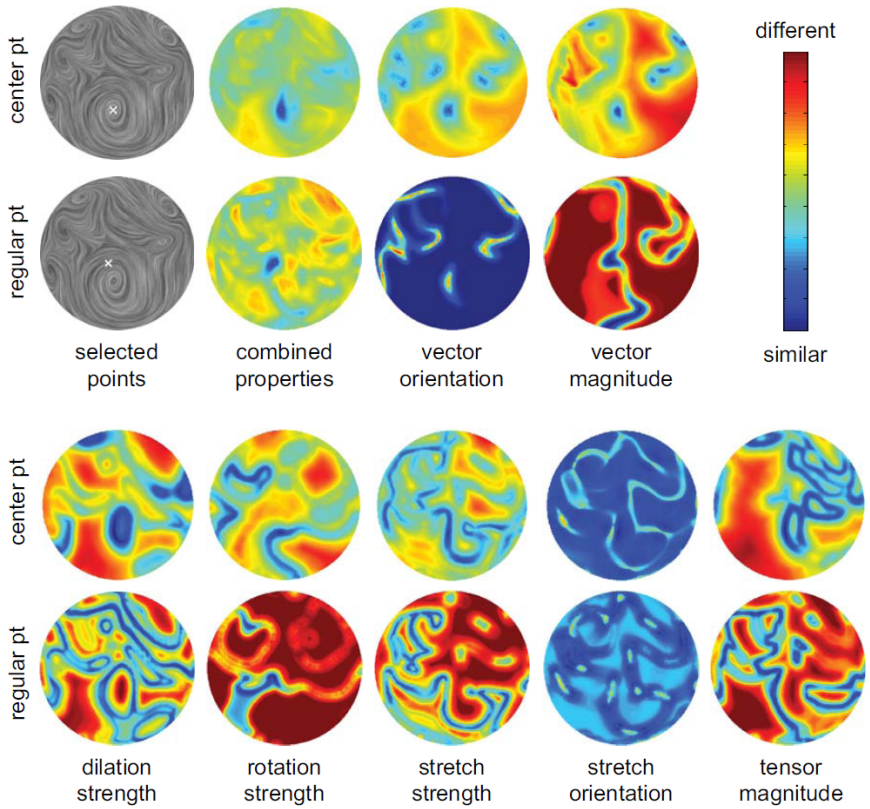

Fig. 1: Tracking flow features by treating a stack of vector fields as spin images and using vector and tensor field measurements [27].

2.2 Gradient Comparison

Correlation between a pair of scalar fields has also been defined based on the gradients. The use of the gradients allows the incorporation of the spatial locality into the correlation computation. We now describe two derived fields that compare gradients and discuss their relative merits.

2.2.1 Definitions and Properties

Sauber et al. [22] introduce a gradient similarity measure (GSIM) between two gradient fields ∇f_i and ∇f_j that assumes high values when the gradients have similar magnitude and direction. The measure is defined at each point as

$$
\begin{aligned}
s(\nabla f_i, \nabla f_j) &= (s_d(\nabla f_i, \nabla f_j) \cdot s_m(\nabla f_i, \nabla f_j))^r, \text{ where} \\
s_d(\nabla f_i, \nabla f_j) &= \left(\frac{\nabla f_i^T \nabla f_j}{\| \nabla f_i \| \cdot \| \nabla f_j \|} \right)^2, \text{ and} \\
s_m(\nabla f_i, \nabla f_j) &= 4 \frac{\| \nabla f_i \| \cdot \| \nabla f_j \|}{(\| \nabla f_i \| + \| \nabla f_j \|)^2}.
\end{aligned}
$$

In the above expression, s_d represents the similarity in gradient direction, s_m represents the similarity in gradient magnitude, and the exponent r is a parameter that determines the sensitivity of the measure. The fields are normalized to have a common range before computing gradients.

Edelsbrunner et al. [3] define a derived field that assumes high values when the gradients are orthogonal to each other. The derived field, denoted by κ, is essentially the length of the cross product between the two gradients vectors.

While the two fields are different in the sense that GSIM measures similarity whereas κ measures dissimilarity, both derived fields have many similarities besides the fact that both are based on gradient comparison. Both GSIM and κ depend on the scale and length of the gradients, are pointwise comparisons, and do not distinguish between positive and negative correlation. The similarities imply that both techniques are applicable to the same data sets. Gosink et al. [5] also compute correlation between gradient fields to study the interactions between the different pairs of scalar fields in multifield data. The inner product of the gradients of two fields of interest is computed over principle level sets of a third field. They employ this approach to study combustion in methane and hydrogen. The correlation field proposed by Gosink et al. is similar to GSIM described above with the difference being the domain over which the correlation field is computed.

2.2.2 Applications

Figure 2 shows the derived field GSIM for two pairs of quantities measured in the simulation of hurricane Isabel. The transfer function assigns non-zero opacity to regions with values of GSIM greater than 0.9. Patterns in the derived field can help in the analysis of various phenomena like fronts in the hurricane.

A visualization of κ helps in the study of the different phases in a combustion simulation as shown in Figure 3. Three time steps are shown: the ignition, burning, and the final phase. The flame front is tracked by regions with large values of κ computed for the scalar field pair `prog` and H_2, which represent the progress of combustion and fuel concentration, respectively. The higher peaks in the terrain

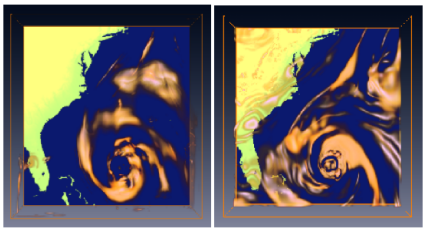

Fig. 2 Gradient similarity measure (GSIM) computed for two pairs of scale fields: precipitation *vs* vapour (left) and vapour *vs* temperature. Image courtesy of Sauber et al. [22].

correspond to sections of the flame front that are progressing faster. They also discuss an application to the study of a protein-protein complex in structural biology. A protein-protein complex consists of two or more proteins docked in a stable conformation. For example, the barnase-barstar complex (1BRS) consists of two proteins. The electrostatic potential defined by barnase (N) and barstar (S) individually in their docked conformation and the potential defined by the complex are available as scalar fields sampled over the space, namely f_N, f_S, and f_{1BRS}. Regions where κ between f_N and f_S is high correspond to salt bridges/strong hydrogen bonds. Figure 4 shows a visualization of κ. The colored dots in the figure indicate high values of κ values, namely those in the range $[0.002, 0.0207]$ and are mapped from blue to red. The dots with values lower than 0.002 are not displayed. The gold lines indicate the hydrogen bonds corresponding to those regions of space.

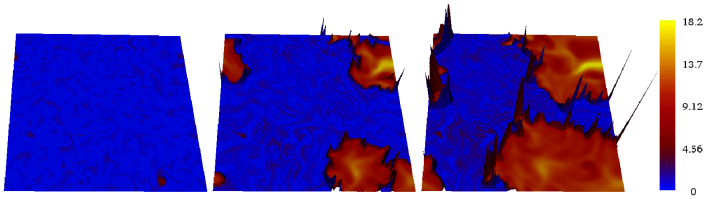

Fig. 3: Local comparison of two scalar fields `prog` and H_2 from a combustion simulation. The derived field κ, which compares the gradients of the two scalar fields, is shown using a terrain map and `prog` is mapped to color. From left to right: ignition phase, burning phase, and the end of combustion. The fronts of the flames are tracked by a region with higher values of κ. This region is represented by the peaks that enclose the burnt region. Image courtesy of Edelsbrunner et al. [3].

3 Alignment and Dependency Measures

We now discuss derived fields that capture the variation or dependency between multiple (greater than two) fields.

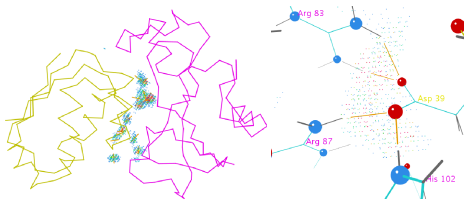

Fig. 4: Visualization of the derived field κ between electrostatic potentials defined by barnase and barstar in the complex 1BRS. Left: an overview of the regions with high values of κ in the complex. The proteins are shown as alpha-carbon traces, with barnase in magenta and barstar in yellow. Bottom: a closeup of a hydrogen bond cluster. `Asp 39` of barstar hydrogen bonds with `Arg 87`, `Arg 83`, and `His 102` of barnase. All four residues are highly important in the interaction between barnase and barstar. Image courtesy of Edelsbrunner et al. [3].

3.1 Local Gradient-Based Comparison Measures

The gradient comparison measures discussed in the previous section also extends to multiple scalar fields. We now describe these extensions, their properties and applications.

3.1.1 Definitions and Properties

The gradient similarity measure GSIM is extended to k gradient fields by computing the minimum gradient pair similarity

$$C_k = \min\{s(\nabla f_i, \nabla f_j) \,|\, 1 \leq i < j \leq k\}.$$

The measure assumes low values if the gradient directions are equally distributed in the domain. Given k fields, GSIM can be computed for all possible subsets of fields. The size of this set grows exponentially with the number of fields and hence it is impractical to compute and analyze GSIM for all subsets of fields. Sauber et al. [22] address this issue by introducing the multifield-graph. Nodes of this graph correspond to each subset of input fields and are displayed with icons that graphically represent the similarity between the fields. Nodes are laid out in layers corresponding to the number of fields in the subset. Two nodes in adjacent layers are connected by an edge if the fields in lower layer node are also compared in the upper layer node. The correlation/similarity and the size of domain with high correlation/similarity are represented by the size and color of a disk displayed within each node. A selective display of nodes enables focusing on nodes that represent high correlations.

The derived field κ also extends to multiple fields. Given k scalar fields, κ is defined as the norm of the wedge product between the 1-forms $\mathrm{d}f_i$,

$$\kappa = \| \, \mathrm{d}f_1 \wedge \mathrm{d}f_2 \wedge \ldots \wedge \mathrm{d}f_k \, \| \, .$$

Each one form $\mathrm{d}f_i$ corresponds to the gradient ∇f_i. The wedge product is a natural extension of the cross product of two gradient vectors and represents the k-dimensional volume of the parallelpiped spanned by the k gradients [3]. While the comparison measure κ does not satisfy the triangle inequality, it satisfies a number of useful algebraic properties.

1. Symmetry: $\kappa(\ldots,f_i,\ldots,f_j,\ldots) = \kappa(\ldots,f_j,\ldots,f_i,\ldots)$.
2. Degeneracy: $\kappa(F) = 0$ if $\mathrm{d}f_i = \mathrm{d}f_j$ for $1 \leq i \neq j \leq k$.
3. Scaling: $\kappa(\alpha f_1 + \beta, f_2, \ldots, f_k) = |\alpha| \cdot \kappa(f_1, f_2, \ldots, f_k)$, with $\alpha, \beta \in \mathbb{R}$.
4. Sub-additivity: $\kappa(f_1 + g_1, f_2, \ldots, f_k) \leq \kappa(f_1, f_2, \ldots, f_k) + \kappa(g_1, f_2, \ldots, f_k)$.
5. Sub-multiplicativity: $\dfrac{\kappa(f_1,\ldots,f_i,f_{i+1},\ldots,f_k)}{\mathrm{vol}(\mathbb{M})} \leq \kappa(f_1,\ldots,f_i) \cdot \kappa(f_{i+1},\ldots,f_k)$.

3.1.2 Computation and Applications

In practice, the scalar fields are measured at discrete points in the domain and linearly interpolated within elements in a triangulation of the manifold. In such a setting, GSIM and κ can be computed in a loop over the d-simplices in the triangulation. Since all functions are linear over a d-simplex, their gradients/differentials are constant within each mesh element. The norm of the k-form is evaluated at a point within the d-simplex directly from the formula and weighted by the volume of the d-simplex.

In a typical application of the multifield-graph, the user selects a particular node using a visual interface and analyzes the derived field corresponding to that particular node. Figure 5 shows the multifield-graph for the hurricane Isabel data set with six scalar fields. Selected nodes are displayed within three of the five possible layers. The extension of κ to k fields is directly visualized for two- and three-dimensional domains to study the relationship between the fields.

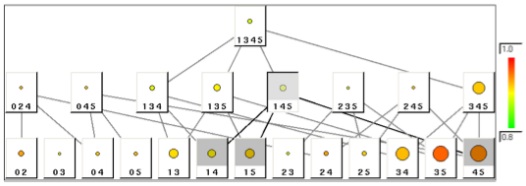

Fig. 5 Multifield-graph computed for the hurricane Isabel data set. The size and color of the disks represent the degree of correlation/similarity between the fields. Image courtesy of Sauber et al. [22].

3.2 Local Statistical Complexity

Multifield data have also been studied using statistical and information theoretic methods. Jänicke et al. [10] adapt the notion of local statistical complexity to the

context of time-varying fields and apply it to study data available from PDE simulations [11]. The local statistical complexity is a measure of the amount of information required from the past to predict the field in the current time step a specific point. It is computed using the notion of entropy and mutual information as a time-varying scalar field. Consider a time-varying field. All points that could possibly influence the value of the field at a point p are arranged into a light cone. The size of the region of influence increases by one for each time step away from p. A light cone (l^+) into the future time steps is also considered, similar to the light cone in the past (l^-), for the computation. A conditional distribution $P(l^+|l^-)$ can be defined on the light cones. The local statistical complexity is computed as the mutual information between the distribution represented by a particular light cone and the equivalence class of past light cones that have similar conditional distribution. Jänicke et al. [10, 11] describe efficient algorithms to compute the local statistical complexity. Features are identified as complex if the probability that they occur again is low. They demonstrate applications of this derived field to a wide range of data from diffusion, flow, and weather simulations.

3.3 Multifield Comparison Measure

Nagaraj and Natarajan introduced a gradient-based comparison measure for multiple scalar fields [14]. The measure is defined as the norm of a matrix comprising the gradient vectors of the different functions. Let A be a $m \times n$ matrix of real numbers. The *norm* of the matrix A, denoted as $\|A\|$, is defined as

$$\|A\| = \max_{\|x\|=1,\, x\in\mathbb{R}^n} \|Ax\|,$$

where $\|x\|$ represents the Euclidean norm of vector x [9]. Let $F = \{f_1, f_2, f_3, \ldots, f_m\}$ be a set of smooth scalar fields defined on a manifold $\mathbb{M}$. The derivative at a point $p \in \mathbb{M}$ is written as a matrix of partial derivatives,

$$dF(p) = \begin{bmatrix} \frac{\partial f_1}{\partial x_1}(p) & \cdots & \frac{\partial f_1}{\partial x_n}(p) \\ \vdots & \ddots & \vdots \\ \frac{\partial f_m}{\partial x_1}(p) & \cdots & \frac{\partial f_m}{\partial x_n}(p) \end{bmatrix}$$

The *multifield comparison measure* η_p^F at point p is defined as the norm of the matrix $dF(p)$, $\eta_p^F = \|dF(p)\|$.

3.3.1 Properties and Computation

The measure η_p^F satisfies three important properties: symmetry, coordinate system independence and stability.

- **Symmetry.** The measure is independent of the permutation of the functions in F.
- **Coordinate system independence**. The norm of the matrix dF at a point p does not depend on the coordinate system used to represent p.
- **Stability.** A finite change in the functions results in a bounded change in the multifield comparison measure. The amount of change additionally depends on the size of the triangle.

Evaluating the multifield comparison measure at a point requires the solution to a maximization problem. Nagaraj and Natarajan show that this computation can be reduced to the faster evaluation of the maximum eigenvalue of a positive semi-definite matrix $\Lambda = (dF(p))^T(dF(p))$

$$\begin{aligned}\eta_p^F &= \left(\max_{x\in\mathbb{R}^n, \|x\|=1} x^T \Lambda\, x\right)^{\frac{1}{2}} \\ &= \max\{\sqrt{\lambda} : \lambda \text{ is a diagonal element of } \Lambda\} \\ &= \max\{\sqrt{\lambda} : \lambda \text{ is an eigenvalue of } (dF(p))^T(dF(p))\}.\end{aligned}$$

The derivative matrix $dF(p)$ is constant within each mesh element if the scalar field is available as a sample and linearly interpolated within elements of a triangulation.

3.3.2 Applications

The multifield comparison measure has been applied to study various real-world data from weather modeling, climate simulations, and combustion simulations. In particular, it was used to study a simulation of the hurricane Isabel and the analysis of a global wind pattern data set.

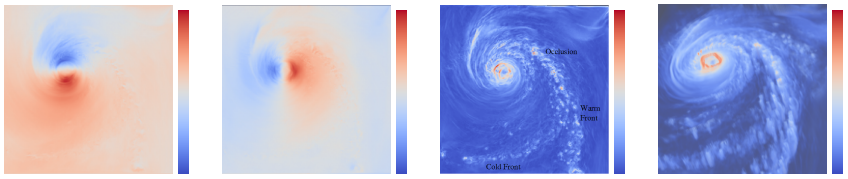

(a) (b) (c) (d)

Fig. 6: Fronts in Hurricane Isabel at hour 40. (a) Volume rendering (top view) of horizontal wind speed Uf. (b) Volume rendering (top view) of horizontal wind speed Vf. (c) Volume rendering (top view) of multifield comparison measure η^F computed for Uf and Vf showing the rainbands at different fronts. The cold front leads the warm front resulting in an occlusion. (d) Volume rendering from a different viewpoint. Image courtesy of Nagaraj and Natarajan [14].

Rainbands and fronts. A simulation of the hurricane Isabel that struck the Atlantic region in USA was performed on a physical area of 2139km $\times$2004km $\times$19.8 km over 48 simulated hours [26]. The data is available over a $600 \times 600 \times 600$ grid

over 48 time steps. Among the multiple quantities computed, the scalar fields corresponding to pressure (Pf) and the horizontal wind velocity components (Uf and Vf) were considered in this experiment. Cloud structures associated with an area of rainfall, called rainbands, occur mainly at boundaries separating two masses of air of different densities and temperatures, called fronts. The leading edge of the cooler mass of air is called the cold front and the leading edge of a warm air mass is called the warm front. The turbulence of the horizontal wind velocity is high near rain bands. The fronts can be analyzed by computing the multifield comparison measure for the pair of 3D scalar fields Uf and Vf, where the 3D domain corresponds to the volume in the altitude range 1500m-5800m.

First, the multifield comparison measure is computed for the fields Uf and Vf in the 10^{th} time step. A visualization of the measure clearly shows the two warm fronts and a cold front [14]. The warm front leads the cold front. This information about fronts cannot be extracted from the two functions individually. The multifield comparison measure is computed next for the fields Uf and Vf in the 40^{th} hour of simulation. The warm front at the north disappears, see Figures 6c and 6d. The previously leading warm front is overtaken by the cold front resulting in an occlusion.

Wind patterns. Prevailing winds blow in a dominant direction at a particular point and are affected by movements in the Earth's atmosphere. In regions of mid-latitudes, the winds blow from west to the east and are known as westerlies. The winds found in the tropics near the equator are easterlies or trade winds. Data from a climate simulation for a 50 year period between 1960 and 2009 is available over 600 time steps corresponding to each month [21]. Data within each time step is available on a 3D grid with resolution corresponding to $1^\circ \times 1^\circ \times 16 plev$ (pressure elevations) on earth.

The wind velocity on the grid is a vector field. The matrix norm for 600 vector fields is computed by replacing the rows with the wind velocities. The norm η^F measures the variation of the wind velocities over the time period of the simulation, see Figure 7b. Comparing with the wind patterns in Figure 7a, we see that high values of η^F correspond to the prevailing winds, particularly the westerlies found in the regions surrounding Antarctica, the region of hurricanes in Atlantic, the cyclone prone region between Madagascar and Australia, and the trade winds across the Atlantic sea traveling towards the Caribbean sea. The distribution of the comparison measure over the isobar for pressure level 300 hPa, which corresponds to approximately 30000 feet above sea level, is shown in Figure 7c. The comparison measure assumes high values over the temperate regions corresponding to the westerly jet. This is a semi-permanent feature of the mid-latitudes. Many regions in the tropics undergo a seasonal reversal of wind (called the monsoons). Lower values of the comparison measure over the tropics indicates unsteadiness and corresponds to a seasonal reversal in wind pattern over this part of the world.

Storm tracks. The regions over the ocean with warm temperatures ($> 27^\circ$C) are susceptible to storms. Filtering out regions with lower temperatures and restricting the analysis to the months from June to November helps locate storm tracks. Regions shown in blue in Figure 7e have been filtered out. The red regions match closely with

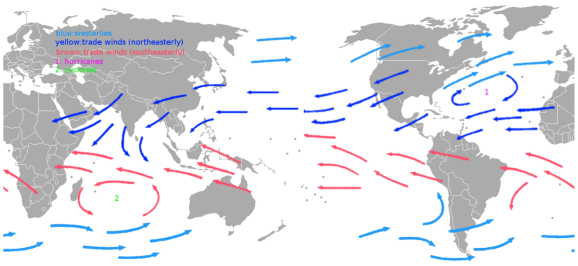

(a)

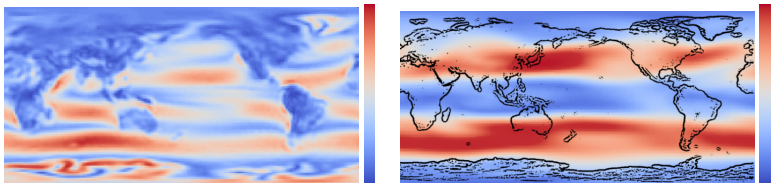

(b) (c)

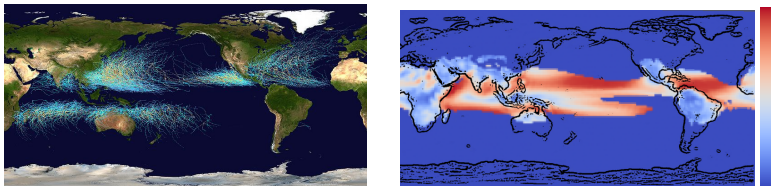

(d) (e)

Fig. 7: Multifield comparison measure η^F computed for wind velocities over the years 1960-2009, where the comparison is over a set of six hundred 3D vector fields. (a) Map of world showing wind patterns (source: Wikipedia) (b) Distribution of η^F over surface corresponding to pressure elevation 925 hPa. The dark red regions correspond to the wind patterns. (c) Distribution of η^F over surface corresponding to pressure elevation 300 hPa. The temperate regions exhibit higher values. (d) Storm track for the years 1985-2005 (source: Wikipedia) (e) Distribution of η^F after removing regions with low mean temperature ($< 27°$C). Red regions correspond to the storm tracks. The world map is overlaid for clarity. Image courtesy of Nagaraj and Natarajan [14].

the storm tracks shown in Figure 7d. Even though the west coast of South America has trade winds, storms are particularly absent due to lower temperatures. The storm prevalent regions in the Indian, Atlantic, and Pacific oceans have high values of the comparison measure.

4 Decomposition and Componentization

In this section we examine a different situation in which multiple fields can arise as the components of a decomposed field.

4.1 Hodge Decomposition

A classical example of this is the Hodge-Helmholtz decomposition [18, 25] of a vector field V as follows:

$$V = V_c + V_d + V_h \tag{1}$$

where V_c is *curl-free* ($\bigtriangledown \times V_c = 0$), V_d is *divergence-free* ($\bigtriangledown \cdot V_d = 0$), and V_h is *harmonic* ($\bigtriangledown \cdot V_h = 0$ and $\bigtriangledown \times V_h = 0$).

Such a decomposition can have applications in many scientific and engineering domains such as fluid simulation and modeling, electromagnetism, weather prediction, engine design, scientific visualization, and computer graphics. In these applications, one often needs to analyze an input vector field such as the velocity of fluid particles and the direction of the magnetic field. One of the most important aspects of a vector field is *singularities*, which are points in the domain that satisfy $V(\mathbf{p}) = 0$. A singularity can be classified by its *Jacobian* (gradient tensor) as follows [6]:

1. source: both eigenvalues of the Jacobian are positive.
2. sink: both eigenvalues are negative.
3. center: both eigenvalues are imaginary numbers.
4. saddle: one of the eigenvalues is positive and the other negative.

Through the decomposition, the sources, sinks, and some saddles can be captured by the curl-free component, while the centers and some other saddles are captured by the divergence-free component. The harmonic component is often seemingly featureless in the planar case. However, on hyperbolic surfaces, the harmonic component can capture the saddles that arise as a result of surface topology. For example, any smooth vector field on a genus-two surface must contain at least four saddles or some higher-order saddles.

Polthier and Preuss develop techniques to efficiently perform Hodge-Helmholtz decomposition a triangular mesh with a piecewise constant vector field [18, 19] (Figure 8). Such techniques are later extended to volumes [25].

Another important application of Hodge-Helmholtz decomposition is in fluid simulation. In this case the fluids are assumed to divergence-free. However, numerical solvers often introduce errors which lead to flow fields with a non-zero divergence, thus causing unrealistic fluid behaviors. This is corrected by a *projection* step, for which the Hodge-Helmholtz decomposition is performed on the vector field, and the curl-free part is removed [23, 24].

4.2 Components of tensor field

There has been some recent trend in studying asymmetric tensor fields [29, 28, 1, 13], with applications in flow visualization and earthquake engineering. Given a vector field V such as the velocity of fluid particles or the deformation of land, the

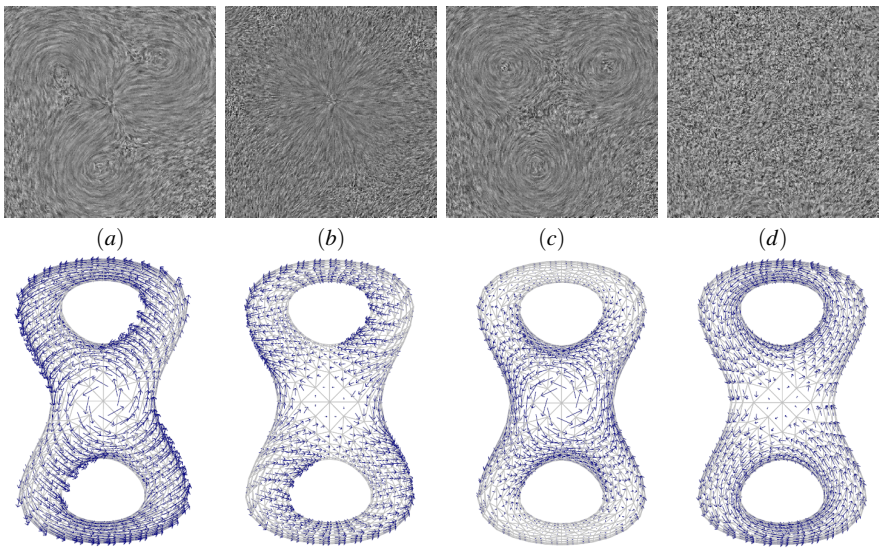

Fig. 8: Two examples of Hodge-Helmholtz decomposition: (top) a planar vector field, and (bottom) a vector field defined on a torus. From left to right are: (a) the original field V, (b) the curl-free component V_c, (c) the divergence-free component V_d, and the harmonic component V_h. Notice that singularities in the original field can be captured effectively by the decomposition. Moreover, the harmonic component is more prominent for fields defined on a hyperbolic manifold. Image courtesy of Polthier and Preuss [18, 19].

gradient $T = \bigtriangledown V$ is an asymmetric tensor field which can be used to describe the deformation of particles in both fluid and solid movements. This can be explained by the following decomposition of the gradient tensor:

$$T = D + R + S \tag{2}$$

where $D = \gamma_d Id$ is a multiple of the identity matrix, R is an anti-symmetric matrix, and S is a *traceless*, symmetric matrix. There are three fundamental fluid motions besides translation, and they are *isotropic scaling*, *rotation*, and *anisotropic stretching* or *pure shearing*. Interesting these motions correspond to the three components described in Equation 2. D describes the isotropic stretching. When $\gamma_d > 0$, the particle's volume will increase, while when $\gamma_d < 0$, the particle will lose volume when it travels. R represents rotations, i.e., spinning around the center of the particle. This is related to the *vortices* in the flow. S corresponds to the anisotropic stretching or stretching. In this case the particle is under *pure shearing*, which refers to simultaneous expansion along some axis or axes and contraction along perpendicular directions without changing the volume. Pure shearing is linked to the rate of angular deformation, rate of mixing of multiple interacting fluid materials, and energy dissipation.

While these fields can be studied independently, in this context it is often important to study their interaction. For example, for two-dimensional cases, i.e., T is a 2×2 matrix, Zhang et al. [28] introduce the notion of *eigenvalue manifold* and *eigenvector manifold*. We will examine these concepts in detail.

In 2D, the components in Equation 2 can be written as follows:

$$D = \gamma_d \begin{pmatrix} 1 & 0 \\ 0 & 1 \end{pmatrix}, \quad R = \gamma_r \begin{pmatrix} 0 & -1 \\ 1 & 0 \end{pmatrix}, \quad S = \gamma_s \begin{pmatrix} \cos\theta & \sin\theta \\ \sin\theta & -\cos\theta \end{pmatrix} \tag{3}$$

where γ_d, γ_r, and $\gamma_s \geq 0$ are the strengths of isotropic scaling, rotation, and pure shearing, respectively. θ decodes the orientation of the shearing. Note the the eigenvalues of T is purely decided by γ_d, γ_r, and γ_s. Zhang et al. [28] treat the triple $(\gamma_d, \gamma_r, \gamma_s)$ as a vector and consider the configurations corresponding to unit vectors. Such vectors form a hemisphere which they refer to as the eigenvalue manifold (Figure 9 (left)). There are five canonical points on this manifold (Figure 9: colored dots), corresponding to $(\gamma_d = 1, \gamma_r = 0, \gamma_s = 0)$ (pure expansion), $(\gamma_d = -1, \gamma_r = 0, \gamma_s = 0)$ (pure contraction), $(\gamma_d = 0, \gamma_r = 1, \gamma_s = 0)$ (pure counterclockwise rotation), $(\gamma_d = 0, \gamma_r = -1, \gamma_s = 0)$ (pure clockwise rotation), and $(\gamma_d = 0, \gamma_r = 0, \gamma_s = 1)$ (pure shearing). A configuration is said to be dominated by one of these five canonical motions, μ, if the point corresponding to the this configuration has the smallest geodesic distance to the canonical motion μ. The partition of the eigenvalue manifold in turns leads to a partition of the domain of tensor field T, although the map is not bijective.

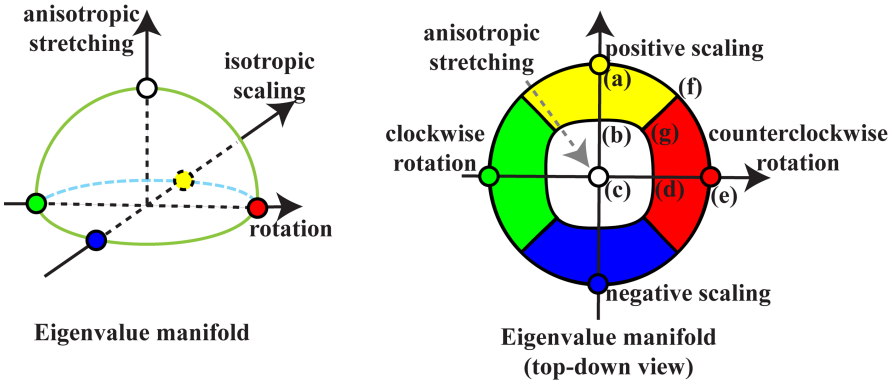

Fig. 9: Eigenvalue Manifold: there are five special points on the manifold, which are positive and negative scaling, counterclockwise and clockwise rotation, and anisotropic stretching. The Voronoi decomposition with respect to these five special points partitions the manifold into five cells where the flow is dominated by different characteristics [28].

Figure 10 illustrates this with an example vector field that is generated by combining two counter-rotating Sullivan vortices. Notice that the flow is predominantly expanding in the middle (yellow), contracting on the outside (blue), rotating (red

and green), and pure shearing (white). Note that a region of predominant expansion motion cannot be directly adjacent to a region of predominant contraction. Similarly, a counterclockwise rotation region cannot be adjacent to a region dominated by clockwise rotation. Such results have led Lin et al. [13] to define asymmetric tensor field topology in terms of graphs whose nodes correspond to the regions in the partition and whose edges encode adjacency relationships between the regions.

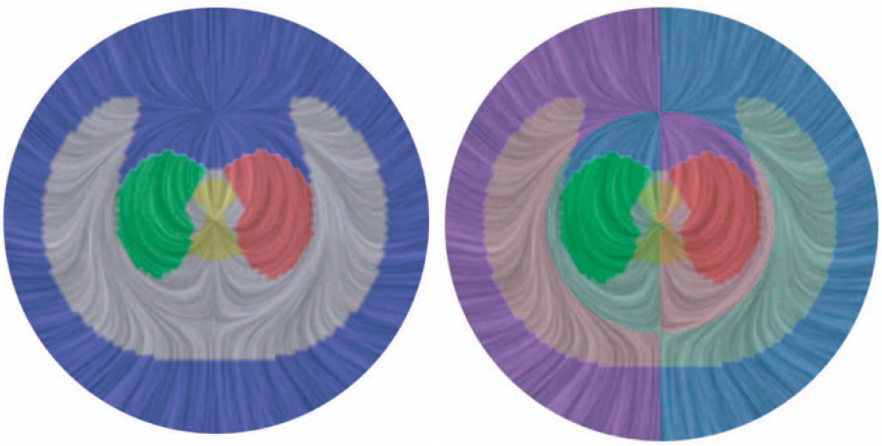

Fig. 10: Coloring coding based on the eigenvalue manifold (left) and the combined eigenvalue and eigenvector manifold (right) [28].

The eigenvector information in the tensor field is determined purely by γ_r, γ_s, and θ from Equation 3. Note that asymmetric tensors may have real eigenvalues (real domains) or complex eigenvalues (complex domains). In the latter case no real-valued eigenvectors exist. Zheng and Pang [29] introduce the notion of *dual-eigenvectors* which they show are the continuous extension of major and minor eigenvectors from the real domains into complex domains. Dual-eigenvectors are also the semi-axes of the elliptical flow patterns inside the complex domains.

Zhang et al. [28] realize that the decomposition from Equation 3 can be simplified and reparameterized as follows:

$$T(\rho,\theta,\varphi) = \rho\cos\varphi \begin{pmatrix} \cos\theta & \sin\theta \\ \sin\theta & -\cos\theta \end{pmatrix} + \rho\sin\varphi \begin{pmatrix} 0 & -1 \\ 1 & 0 \end{pmatrix} \tag{4}$$

where $\rho = \sqrt{\gamma_r^2 + \gamma_s^2}$ is the tensor magnitude. Notice that D, the isotropic scaling component, does not impact the directional information in a tensor field and can be dropped when considering eigenvectors. Furthermore, (γ_s, γ_r) is considered as a vector since it is their respective strength that determines whether a tensor is in the real domain or complex domain, the angle between the major and minor eigenvectors in the real domain, and the eccentricity of the elliptical flow patterns in the complex domain. Similar to the definition of eigenvalue manifold, Zhang et al. define the

eigenvector manifold by consider unit vectors, i.e., $\gamma_r^2 + \gamma_s^2 = 1$. Such tensors can be parametrized using spherical coordinates shown in Equation 4. Zhang et al. [28] demonstrate that a tensor is in the real domain if $-\frac{\pi}{4} < \phi < \frac{\pi}{4}$ and complex domain if $\phi < -\frac{\pi}{4}$ or $\phi > \frac{\pi}{4}$. The equator ($\phi = 0$) correspond to the pure shearing tensors while the poles ($\phi = \pm\frac{\pi}{2}$) correspond to pure rotations (degenerate points in the tensor). The boundary between the real and complex domains ($\phi = \pm\frac{\pi}{4}$) is referred to *degenerate curves*. Points on these curves correspond to *simple shears* which are different from pure shears. Notice that equator serves as the boundary between counterclockwise rotating flows and clockwise rotating flows. Figure 11 illustrates these facts, while Figure 12 demonstrates some special configurations.

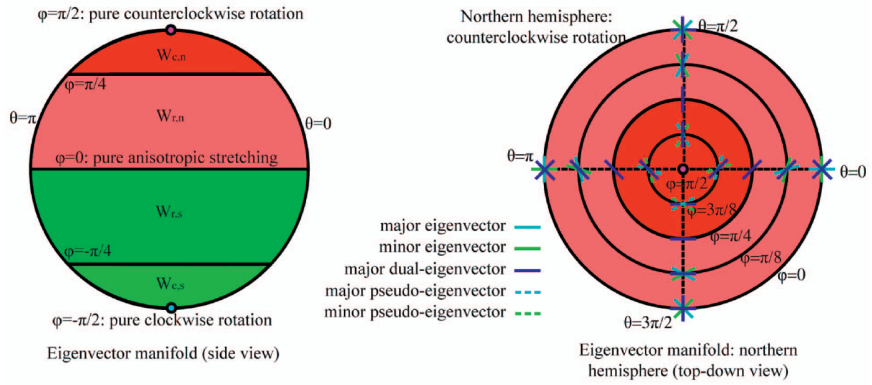

Fig. 11: Eigenvector manifold: the orientation of the rotational component is counterclockwise in the northern hemisphere and clockwise in the southern hemisphere. Each hemisphere is partitioned into real domains and complex domains. The equator represents pure symmetric tensors (irrotational flows), while the poles represent pure rotations. The directions of expansions and contraction in the real domain as well as the orientations of the elliptical patterns are determined by the relative stretches between the rotation and stretching components in the decomposition [28].

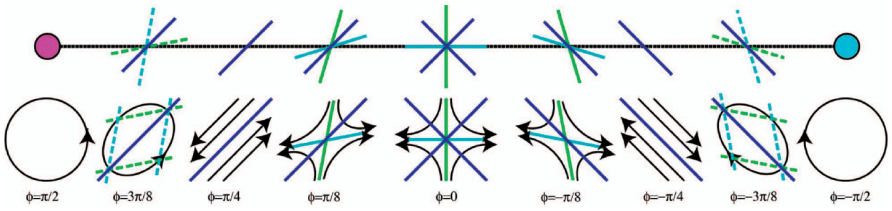

Fig. 12: Example tensors and their corresponding vector field patterns [28].

The decomposition in Equation 4 can also be used to *symmetric* tensor fields. In this case $\gamma_r = 0$ and the tensor can be rewritten as:

$$\rho \sin\phi \begin{pmatrix} 1 & 0 \\ 0 & 1 \end{pmatrix} + \rho \cos\phi \begin{pmatrix} \cos\theta & \sin\theta \\ \sin\theta & -\cos\theta \end{pmatrix} \tag{5}$$

where $\rho = \sqrt{\gamma_d^2 + \gamma_s^2}$ again is the tensor magnitude. Like Equation 4, this equation is a special case of Equation 2 where one of the three components disappears (the anti-symmetric component). Nieser et al. [15] et al. have applied this to the curvature tensor to extract surface features for remeshing purposes. Figure 13 illustrates this classification with a bunny surface.

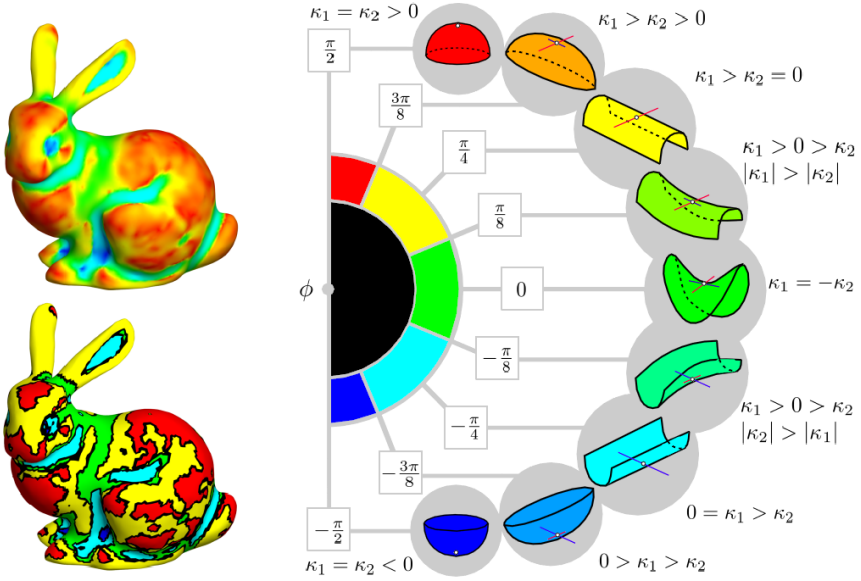

Fig. 13: The tensor decomposition in Equation 4 can be adapted to symmetric tensors. In this example the symmetric tensor is the curvature tensor in the surface. Note that this tensor decomposition can lead to surface classification and feature extraction [15].

4.3 Higher order tensor fields

The decomposition of the asymmetric tensor field is intrinsically linked to the Hodge-Helmholtz decomposition. *D*, *R*, and *S* from Equation 2 correspond to the

curl-free, divergence-free, and harmonic component in the Hodge-Helmholtz decomposition.

Higher-order tensors, i.e., tensors of a rank larger than two, are of great interests to scientists and engineers in many application domains. For example, general relativity deals with higher-order tensors. Elasticity tensor, a fourth-order tensor, relates the strain tensor (deformation) to the stress tensor (force). The spatial gradient of an N-th order tensor is an $N+1$-th order tensor. This has been used by Delmarcelle and Hesselink to classify degenerate points for symmetric second-order tensors [2]. A special class of higher-order tensors have also been used to describe rotational symmetries on surfaces [16], with applications in pen-and-ink sketching [7], remeshing [20, 15], and regular texture and geometry synthesis on surfaces [15].

There have been a number of decomposition methods [12]. However, physical interpretation of these decompositions as well as effective analysis and visualization is still lacking. The only prominent work available at this point is [8].

5 Conclusions

In this chapter we have examined applications and existing techniques on multifield visualization based on the notion of derived fields. The derived fields play an important role in understanding relationships between multiple input fields. In addition, for a single input field, multiple derived fields can be generated as a result of decomposition which have the potential of providing insights on the input field.

There are a number of future research directions that we believe are important and can have major impact on multifield visualization:

1. Adaptation of pairwise similarity/dissimilarity as well as global alignment and dependency measures to a set of heterogeneous fields.
2. A detailed study of the sensitivity of the derived fields to the mesh that represents the domain. This study will be particularly useful if the input fields are specified on different meshes representing a common domain.
3. An effective interface using derived fields that supports identification of (a) important fields that can further analyzed in detail and (b) redundant fields that can be discarded from further studies.
4. Integrating the derived fields with existing techniques for interactive exploration like query-based visualization framework [5], focus+context, and show and brush for visual analysis.

Acknowledgements Natarajan acknowledges support from the Department of Science and Technology, India under grant SR/S3/EECE/048/2007. Zhang is partially supported by National Science Foundation awards IIS-0546881 and CCF-0830808.

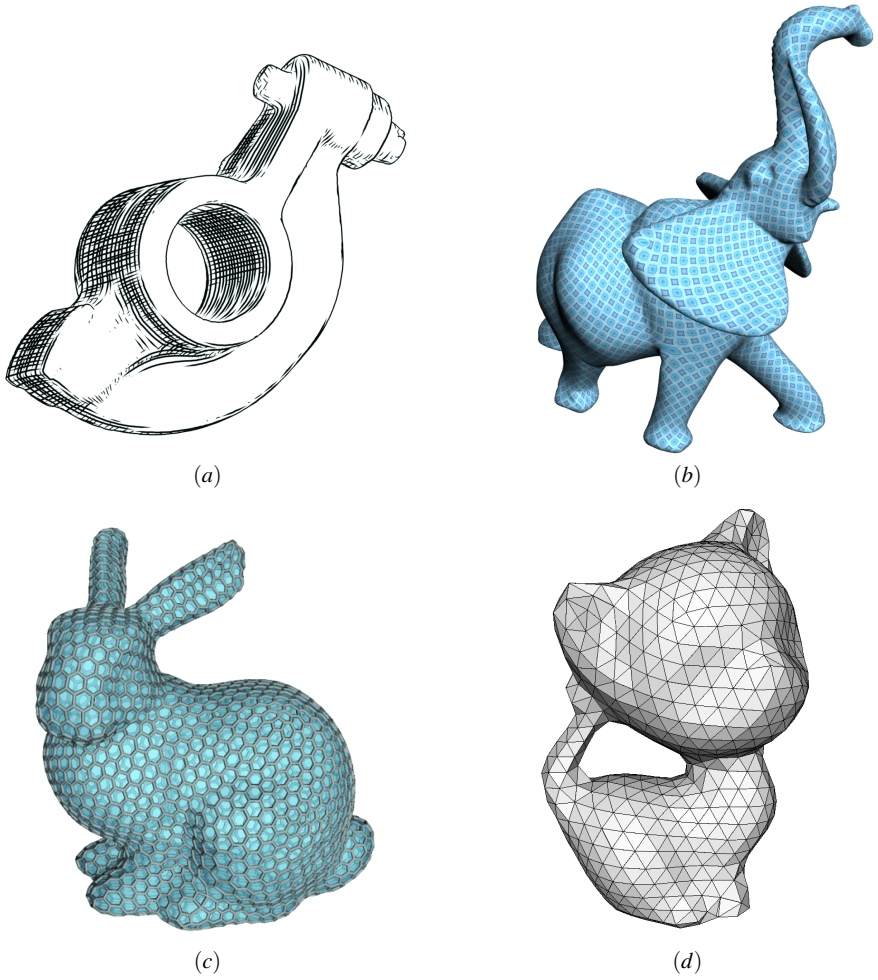

Fig. 14: Higher-order tensors have been used to present N-way rotational symmetries (N-RoSy [16]), with applications in pen-and-ink sketching (a), regular pattern synthesis (b), architectural modeling (c), and geometry remeshing (d). Image (a) and (c) are courtesy of [17].

References

1. Chen, G., Palke, D., Lin, Z., Yeh, H., Vincent, P., Laramee, R.S., Zhang, E.: Asymmetric tensor field visualization for surfaces. IEEE Proceedings on Visualization (2011)
2. Delmarcelle, T., Hesselink, L.: The topology of symmetric, second-order tensor fields. IEEE Computer Graphics and Applications pp. 140–147 (1994)
3. Edelsbrunner, H., Harer, J., Natarajan, V., Pascucci, V.: Local and global comparison of continuous functions. In: Proc. IEEE Conf. Visualization, pp. 275–280 (2004)

4. Feller, W.: An Introduction to Probability Theory and Its Applications. Volume I. John Wiley & Sons, New York (1968)
5. Gosink, L., Anderson J. Bethel, W., Joy, K.: Variable interactions in query-driven visualization. IEEE Transactions on Visualization and Computer Graphics **13**(6), 1400–1407 (2007)
6. Helman, J.L., Hesselink, L.: Representation and Display of Vector Field Topology in Fluid Flow Data Sets. IEEE Computer **22**(8), 27–36 (1989)
7. Hertzmann, A., Zorin, D.: Illustrating smooth surfaces. Computer Graphics Proceedings, Annual Conference Series (SIGGRAPH 2000) pp. 517–526 (2000)
8. Hlawitschka, M., Scheuermann, G.: HOT lines: tracking lines in higher order tensor fields. In: Proceedings IEEE Visualization 2005, pp. 27–34 (2005)
9. Horn, R., Johnson, C.: Matrix Analysis. Cambridge University Press (1985)
10. Jänicke, H., Bottinger, M., Tricoche, X., Scheuermann, G.: Automatic detection and visualization of distinctive structures in 3d unsteady multi-fields. Computer Graphics Forum **27**(3), 767–774 (2008)
11. Jänicke, H., Wiebel, A., Scheuermann, G., Kollmann, W.: Multifield visualization using local statistical complexity. IEEE Transactions on Visualization and Computer Graphics **13**, 1384–1391 (2007)
12. Kolda, T.G., Bader, B.W.: Tensor decompositions and applications. SIAM Review **51**(3), 455–500 (2009)
13. Lin, Z., Yeh, H., Laramee, R.S., Zhang, E.: 2d asymmetric tensor field topology. In: Topological Methods in Data Analysis and Visualization II, (Proceedings of Topo-In-Vis 2011). Springer Verlag (2012)
14. Nagaraj, S., Natarajan, V., Nanjundiah, R.S.: A gradient-based comparison measure for visual analysis of multifield data. Computer Graphics Forum **30**(3), 1101–1110 (2011)
15. Nieser, M., Palacios, J., Polthier, K., Zhang, E.: Hexagonal global parameterization of arbitrary surfaces. IEEE Transactions on Visualization and Computer Graphics (2012)
16. Palacios, J., Zhang, E.: Rotational symmetry field design on surfaces. ACM Trans. Graph. **26**(3), 55:1–55:10 (2007)
17. Palacios, J., Zhang, E.: Interactive visualization of rotational symmetry fields on surfaces. IEEE Transactions on Visualization and Computer Graphics **17**(7), 947–955 (2011)
18. Polthier, K., Preuss, E.: Variational approach to vector field decomposition. In: Scientific Visualization, (Proc. of Eurographics Workshop on Scientific Visualization). Springer Verlag (2000)
19. Polthier, K., Preuss, E.: Identifying vector fields singularities using a discrete hodge decomposition. In: Visualization and Mathematics III, Eds: H. C. Hege, K. Polthier. Springer Verlag (2002)
20. Ray, N., Li, W.C., Lévy, B., Sheffer, A., Alliez, P.: Periodic global parameterization. ACM Transactions on Graphics **25**(4), 1460–1485 (2006)
21. Roeckner, E., Bäuml, G., Bonaventura, L., Brokopf, R., Esch, M., Giorgetta, M., Hagemann, S., Kirchner, I., Kornblueh, L., Manzini, E., Rhodin, A., Schlese, U., Schulzweida, U., Tompkins, A.: The atmospheric general circulation model echam5. part 1: Model description. Tech. Rep. 349, Max Planck Institute of Meteorology (2003)
22. Sauber, N., Theisel, H., Seidel, H.P.: Multifield-graphs: An approach to visualizing correlations in multifield scalar data. IEEE Transactions on Visualization and Computer Graphics **12**(5), 917–924 (2006)
23. Stam, J.: Stable fluids. In: Proceedings of the 26th annual conference on Computer graphics and interactive techniques, SIGGRAPH '99, pp. 121–128. ACM Press/Addison-Wesley Publishing Co., New York, NY, USA (1999). DOI http://dx.doi.org/10.1145/311535.311548. URL http://dx.doi.org/10.1145/311535.311548
24. Stam, J.: Flows on surfaces of arbitrary topology. ACM Transactions on Graphics (SIGGRAPH 2003) **22**(3), 724–731 (2003)
25. Tong, Y., Lombeyda, S., Hirani, A.N., Desbrun, M.: Discrete multiscale vector field decomposition. ACM Trans. Graph. **22**(3), 445–452 (2003)
26. Wang, W., Bruyere, C., Kuo, B.: Competition data set and description in 2004 IEEE Visualization design contest (2004). Http://vis.computer.org/vis2004contest/data.html

27. Xu, K., Cohne-Or, D., Ju, T., Liu, L., Zhang, H., Zhou, S., Xiong, Y.: Feature-aligned shape texturing. ACM Transactions on Graphics, (Proceedings SIGGRAPH Asia 2009) **28**(5), Article 108 (2009)
28. Zhang, E., Yeh, H., Lin, Z., Laramee, R.S.: Asymmetric tensor analysis for flow visualization. IEEE Transactions on Visualization and Computer Graphics **15**(1), 106–122 (2009)
29. Zheng, X., Pang, A.: 2D asymmetric tensor analysis. IEEE Proceedings on Visualization pp. 3–10 (2005)